The Astrophysical Journal, 781:71 (12pp), 2014 February 1 doi:10.1088/0004-637X/781/2/71

DRIFT EFFECTS ON THE GALACTIC COSMIC RAY MODULATION

M. Laurenza[1], A. Vecchio[2,3], M. Storini[1], and V. Carbone[3,4]
[1] INAF/IAPS, Via Fosso del Cavaliere 100, I-00133 Roma, Italy; monica.laurenza@iaps.inaf.it
[2] Istituto Nazionale di Geofisica e Vulcanologia-Sede di Cosenza, I-87036 Rende (CS), Italy
[3] Dipartimento di Fisica, Università della Calabria, I-87036 Rende (CS), Italy
[4] ISAC-CNR, I-88046 Lamezia Terme, Italy
Received 2013 August 9; accepted 2013 December 1; published 2014 January 10

ABSTRACT

Cosmic ray (CR) modulation is driven by both solar activity and drift effects in the heliosphere, although their role is only qualitatively understood as it is difficult to connect the CR variations to their sources. In order to address this problem, the Empirical Mode Decomposition technique has been applied to the CR intensity, recorded by three neutron monitors at different rigidities (Climax, Rome, and Huancayo–Haleakala (HH)), the sunspot area, as a proxy for solar activity, the heliospheric magnetic field magnitude, directly related to CR propagation, and the tilt angle (TA) of the heliospheric current sheet (HCS), which characterizes drift effects on CRs. A prominent periodicity at ∼six years is detected in all the analyzed CR data sets and it is found to be highly correlated with changes in the HCS inclination at the same timescale. In addition, this variation is found to be responsible for the main features of the CR modulation during periods of low solar activity, such as the flat (peaked) maximum in even (odd) solar cycles. The contribution of the drift effects to the global Galactic CR modulation has been estimated to be between 30% and 35%, depending on the CR particle energy. Nevertheless, the importance of the drift contribution is generally reduced in periods nearing the sunspot maximum. Finally, threshold values of ∼40°, ∼45°, and >55° have been derived for the TA, critical for the CR modulation at the Climax, Rome, and HH rigidity thresholds, respectively.

Key words: cosmic rays – methods: data analysis – Sun: activity

Online-only material: color figures

1. INTRODUCTION

It is widely known that Galactic cosmic rays (CRs) are modulated by solar activity (see the pioneering works by Forbush 1954, 1966). In the 100 years since the discovery of CRs (Hess 1912), the topic of CR modulation has been widely investigated (see Potgieter 2013b for an extended review). The different forms of modulation (short-, medium-, and long-term) were identified by a thorough analysis of the available experimental data and interplanetary perturbations were recognized as the sources of the three-dimensional variability of the incoming charged particles in the heliosphere (see, for instance, Storini 1990, 1997). An important source of CR modulation is represented by solar activity, which is variable on a wide range of temporal scales. The main modulation is at 11 yr timescale and it is related to the so-called Schwabe cycle. As a consequence, the CR intensity shows a pronounced 11 yr variation, with the intensity maximum corresponding almost with the solar activity minimum and vice versa. In addition, many manifestations of solar magnetism, as well as some interplanetary phenomena, show quasi-biennial oscillations (QBOs; see Bazilevskaya et al. 2000; Vecchio et al. 2012a and references therein), which are also present in CR measurements (e.g., Laurenza et al. 2012 and references therein). In particular, it has been shown that the main features of solar activity can be essentially described by superposing QBOs to the ∼11 yr mode (e.g., Vecchio et al. 2010; Laurenza et al. 2012). The CR intensity profile also follows a 22 yr cycle with alternate maxima being flat-topped and peaked (e.g., Smith 1990). This peculiar behavior is described by models of CR modulation (Jokipii et al. 1977; Potgieter & Le Roux 1992; Le Roux & Potgieter 1992a, 1992b; Ferreira & Potgieter 2004; Manuel et al. 2011), based on the observed reversal of the Sun's magnetic field polarity, curvature, and gradient drifts in the interplanetary magnetic field. To characterize the polarity state of the Sun's dipole magnetic field, the parameter A, positive when the magnetic field polarity of the northern solar pole is positive and negative in the opposite case, is used. In the drift formalism, during epochs with $A > 0$ the approach in the inner heliosphere of positively charged CRs is from the polar regions while during periods with $A < 0$ the preferred direction of penetration is along the heliospheric current sheet (HCS).

The wavy HCS (e.g., Hoeksema et al. 1982; Jiang et al. 2010) has become a successful physical entity in describing the global Galactic CR modulation. During a solar rotation, the HCS moves by changing its heliographic latitude. The average excursion, measured from the heliographic equator, is referred to as the tilt angle (TA; e.g., Hoeksema et al. 1982), which can be considered as a proxy for drift effects on CRs (e.g., Jokipii & Thomas 1981; Kota & Jokipii 1983; Wibberenz et al. 2001; Strauss et al. 2012) and it is widely used in modeling and data interpretation (e.g., Christon & Stone 1986; Cliver & Ling 2001; El-Borie 2001; Alanko-Huotari et al. 2007; Badruddin et al. 2007). The modulation effects of the HCS and other drifts, the subsequent 22 yr cycle, and the corresponding charge-sign dependence in the inner heliosphere have been investigated by means of theoretical modeling (e.g., Potgieter & Ferreira 2001). In periods of minimum solar activity, i.e., when the CR modulation by solar activity is reduced, the effects related to the polarity state of the heliosphere and the HCS tilt should be more important than in other activity phases.

Vecchio et al. (2012b) found a relevant scale of CR variability at ∼6 yr, unrelated to solar activity perturbations. They suggested that the 6 yr CR variability could be related to the variation of the latitude extent of the HCS during the solar cycle, thus affecting the particle propagation. This variation could play a crucial role in determining the flat-topped maximum of CRs during even sunspot cycles, as expected from drift models (e.g., Kota & Jokipii 1983).

Although drift effects on CR particles are qualitatively well understood, their quantitative contribution remains uncertain. The main reason for this uncertainty is that, typically, the tilt of the HCS changes in phase with the solar activity and with other solar and heliospheric parameters like the magnetic field strength, thus making it difficult to quantify the net contribution of the different effects.

In this paper, we attempt to connect the CR variations at different timescales to their drivers, in order to identify the different roles played in the modulation and to quantify their contribution. We analyze CR measurements, sunspot areas (SAs), HCS TA, and heliospheric magnetic field (HMF) data, in order to isolate drift effects associated with the tilted HCS. In Section 2, we present results obtained by applying Empirical Mode Decomposition (EMD) analysis to the CR and HCS TA data sets. Section 3 describes two reconstructions of the CR signal, using selected EMD modes, and discusses the possible association with the different sources of the CR variability, namely solar activity and drift effects. In Section 4, conclusions are drawn.

2. DATA USED AND METHOD OF INVESTIGATION

Monthly averaged time series derived from records of three neutron monitors at different cutoff rigidities, Climax[5] (CLI, ~3.0 GV cutoff rigidity), Rome[6] (RM, ~6.3 GV cutoff rigidity), and Huancayo–Haleakala[7] (HH, ~12.9 GV cutoff rigidity) have been considered. CLI and HH data coverage is from 1953–2004, while RM data start in 1957 July. The HCS TA,[8] obtained from records at the Wilcox Solar Observatory (WSO), is defined as one-half the sum of the maximum latitudinal excursions (north and south) of the solar neutral line during each Carrington rotation (Hoeksema 1989) and it is available from 1967 May to the present. We use the TA as computed through the "classical" potential field models, based on the line-of-sight boundary condition at the photosphere. We also analyzed the average polar field strength[9] ($B_{\rm avg}$) to represent the background HMF magnitude, directly related to CR propagation. Finally, monthly average SAs[10] have also been considered as a parameter describing solar activity and related interplanetary perturbations that influence the CR modulation. The data are displayed in Figure 1.

To identify the periodicities present in each data set and their relative amplitude, we use the EMD (Huang et al. 1998), a technique developed to process non-linear and non-stationary data. The EMD decomposes each time series into a finite number of intrinsic mode functions (IMFs), which depends on the data set, and a residue by using an adaptive basis derived directly from the data:

$$\Psi(t) = \sum_{j=1}^{m} \psi_j(t) + r_{\rm m}(t). \quad (1)$$

In Equation (1), $\Psi(t)$ is the time series and $\psi_j(t)$ and $r_{\rm m}(t)$ represent the IMFs and the residue, respectively. Each IMF satisfies two conditions: (1) the number of extrema and the zero-crossings are either equal or differ at most by one and (2) at any point the mean value of the lower and upper envelope, formed by the local maxima and the local minima, is zero. In this way, $\psi_j(t)$ represents a zero mean oscillation experiencing amplitude and frequency modulations, namely $\psi_j(t) = A_j(t)\cos[\phi_j(t)]$, where $\phi_j(t)$ is the phase, and $\omega_j(t) = d\phi_j(t)/dt$ is the instantaneous frequency. Each IMF is characterized by a typical timescale τ_j, defined as the average time difference between local extrema of ψ_j. More details about the iterative process used to calculate the IMFs can be found in Vecchio et al. (2010, 2012a). This kind of decomposition is local, complete, and orthogonal (Huang et al. 1998; Cummings et al. 2004). The residue $r_m(t)$ in Equation (1) describes the mean trend when present. The orthogonality property allows one to reconstruct the signal, at a chosen timescale, through partial sums in Equation (1) (see also Terradas et al. 2004). The instantaneous amplitude $A_j(t)$ and frequency $\omega_j(t)$ can be calculated through the application of the Hilbert transform to each IMF, namely

$$\psi_j^*(t) = \frac{1}{\pi} P \int_{-\infty}^{+\infty} \frac{\psi_j(t')}{t - t'} dt', \quad (2)$$

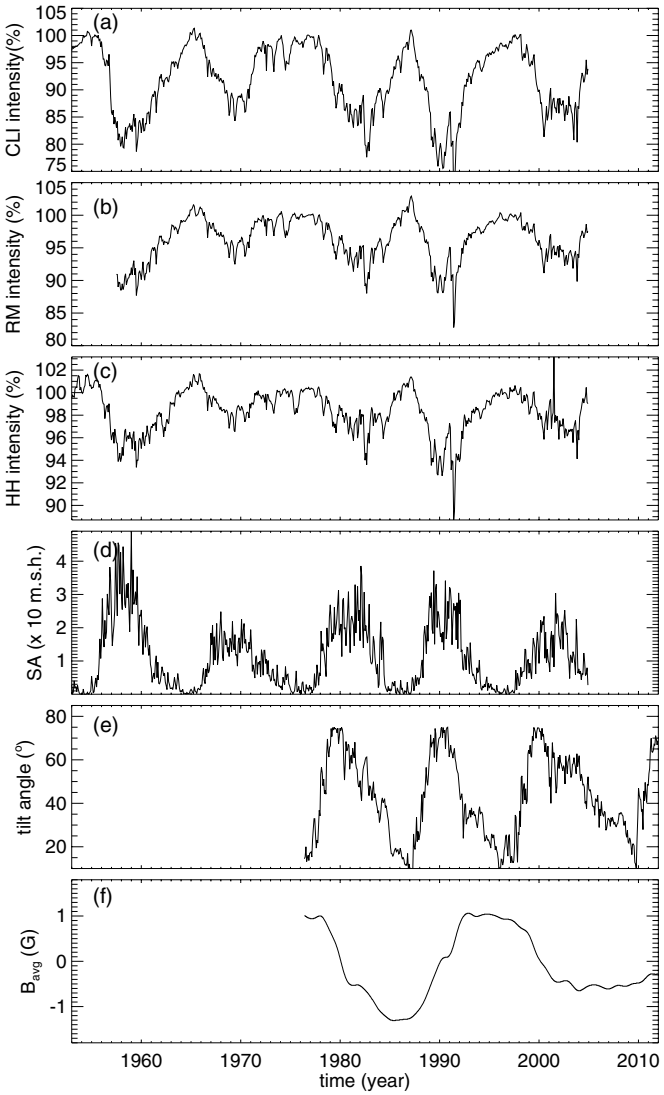

Figure 1. Top to bottom: time history of CR intensity measured at Climax (CLI), Rome (RM), and Huancayo–Haleakala (HH), sunspot area (SA), title angle, and $B_{\rm avg}$, representing the background heliospheric magnetic field magnitude.

[5] http://ulysses.sr.unh.edu/NeutronMonitor/
[6] http://webusers.fis.uniroma3.it/svirco
[7] http://ulysses.sr.unh.edu/NeutronMonitor
[8] http://wso.stanford.edu/Tilts.html
[9] http://wso.stanford.edu/Polar.html. It is calculated from the daily polar field intensities between ~55° and the poles, measured at WSO.
[10] http://solarscience.msfc.nasa.gov/greenwch.shtml

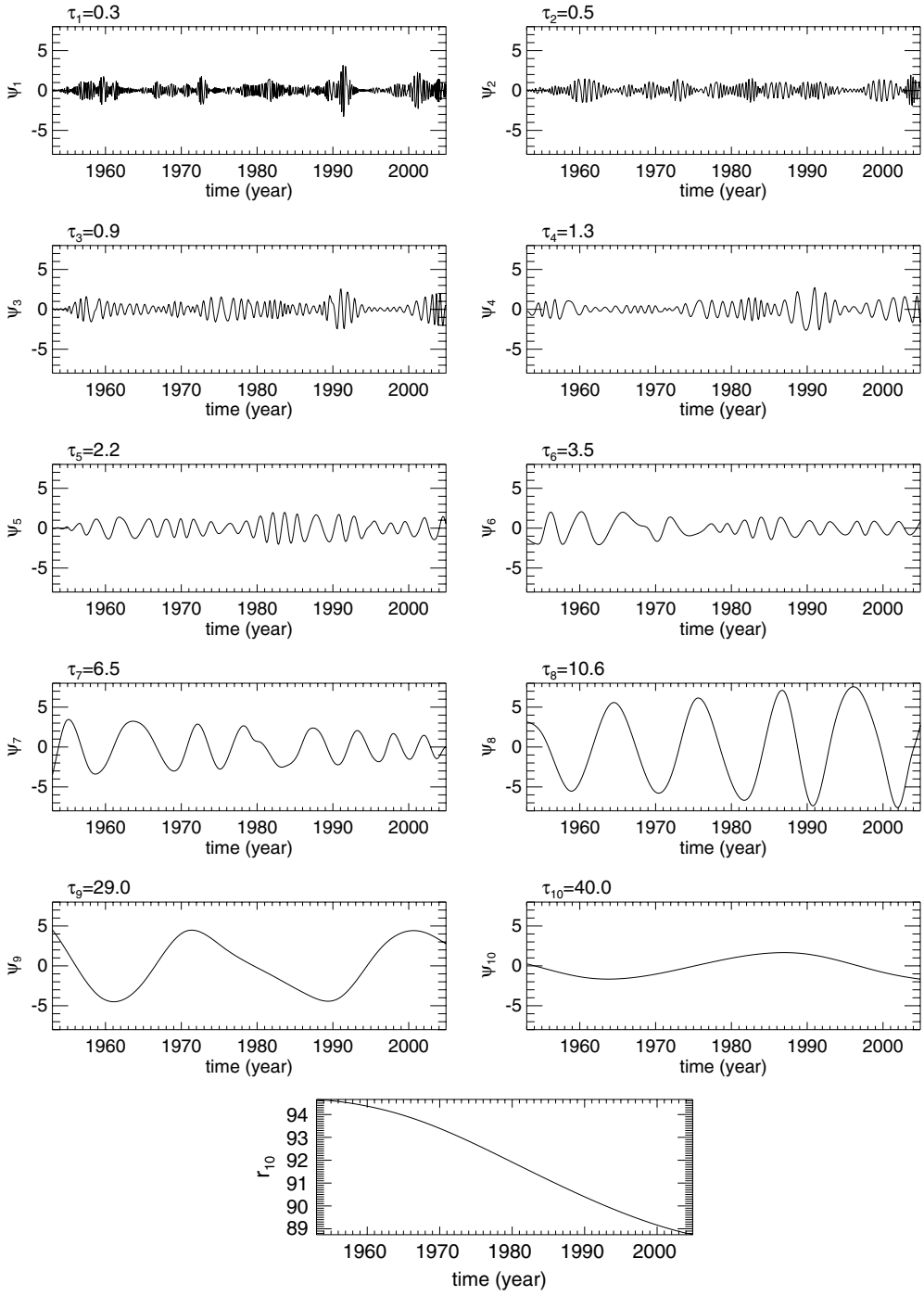

Figure 2. EMD modes (j values from 1–10) and the residue r_{10} for CLI data; τ_j is expressed in yr.

where P indicates the Cauchy principal value and $[\psi_j, \psi_j^*]$ are the complex conjugate pair so that

$$A_j(t) = \left[\psi_j^2 + \psi_j^{*2}\right]^{1/2} \tag{3}$$

$$\omega_j(t) = \frac{d}{dt} \arctan[\psi_j^*/\psi_j] \quad . \tag{4}$$

Figures 2 and 3 show the EMD decomposition of CLI and TA data, for which 10 and 8 IMFs, respectively, were obtained. Table 1 reports, for all records, the number of modes m obtained through the EMD decomposition along with the characteristic timescale of each IMF. The statistical significance of the IMFs has been checked by using the test developed by Wu & Huang (2004) and based on the comparison between the IMFs obtained from the signal and the corresponding ones derived from a white-noise process. This approach represents the analogy of the statistical significance tests used in other common decomposition techniques. For instance, as far as the wavelet power spectra are concerned, theoretical wavelet spectra for white or red noise processes are derived and used to establish significance levels and confidence intervals (e.g., Torrence & Compo 1998). Results from the test performed on the CLI and TA data set are shown in Figure 4 where the dashed, dot–dashed, and dotted lines indicate the spread lines, for the white noise, at the 90th, 95th, and 99th percentile, respectively, and symbols

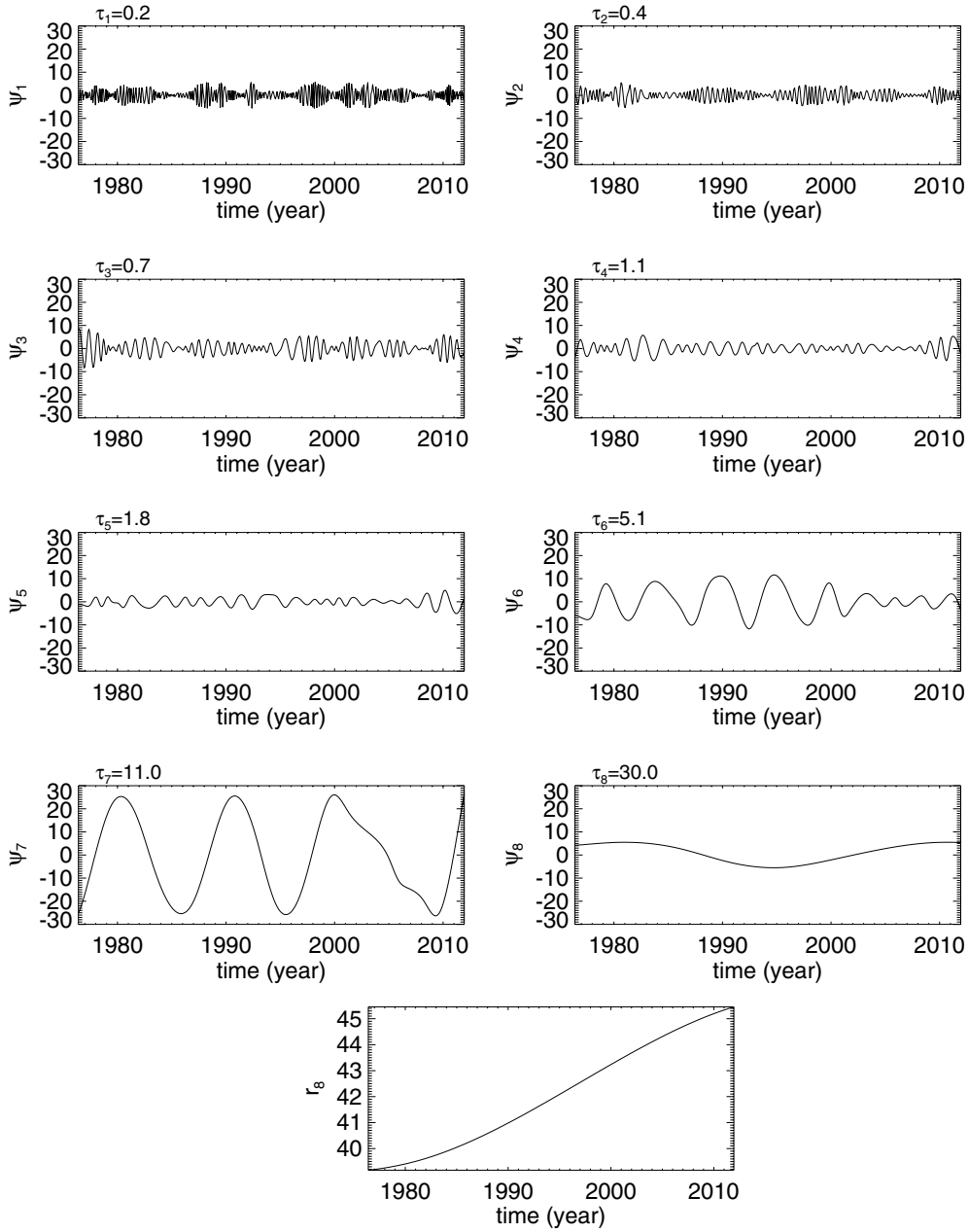

Figure 3. EMD modes (j values from 1–8) and the residue r_8 for TA data; τ_j is expressed in yr.

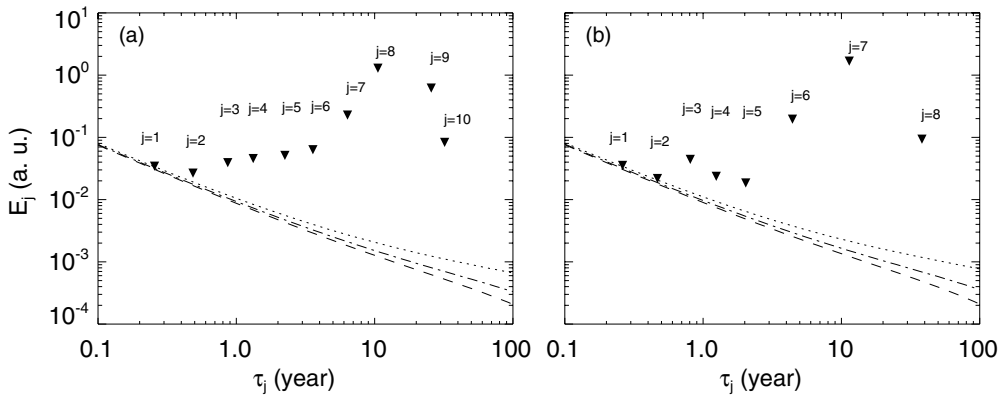

Figure 4. IMF average square amplitude (E_j) vs. typical period (τ_j) for the IMFs from CLI (a) and TA (b). Dashed, dot–dashed, and dotted lines indicate the 90th, 95th, and 99th percentile, respectively.

Table 1
Number (m) of EMD Modes (see Equation (1)) for each Data Set and Their Typical Periods (τ), Calculated as the Average Time Difference Between Local Extrema

Data	m	$\tau < 1$ yr	QBO	$\tau \sim 6$ yr	$\tau \sim 11$ yr	$\tau \sim 22$ yr	$\tau > 22$ yr
CLI	10	$\tau_1 = 0.255 \pm 0.005$ $\tau_2 = 0.48 \pm 0.01$ $\tau_3 = 0.87 \pm 0.02$	$\tau_4 = 1.31 \pm 0.04$ $\tau_5 = 2.19 \pm 0.09$ $\tau_6 = 3.5 \pm 0.3$	$\tau_7 = 6.5 \pm 0.5$	$\tau_8 = 10.6 \pm 0.3$	$\tau_9 = 26 \pm 5$	$\tau_{10} \sim 40$
RM	8	$\tau_1 = 0.252 \pm 0.005$ $\tau_2 = 0.50 \pm 0.01$ $\tau_3 = 1.02 \pm 0.02$	$\tau_4 = 1.6 \pm 0.1$ $\tau_5 = 2.7 \pm 0.1$	$\tau_6 = 5.6 \pm 0.5$	$\tau_7 = 10.4 \pm 0.4$	$\tau_8 = 33 \pm 11$	
HH	10	$\tau_1 = 0.249 \pm 0.004$ $\tau_2 = 0.43 \pm 0.01$ $\tau_3 = 0.77 \pm 0.18$ $\tau_4 = 1.27 \pm 0.49$	$\tau_5 = 2.0 \pm 0.7$ $\tau_6 = 3.9 \pm 2.5$	$\tau_7 = 6.2 \pm 0.5$	$\tau_8 = 11.4 \pm 1.3$	$\tau_9 = 16 \pm 2$ $\tau_{10} = 26 \pm 2$	
TA	8	$\tau_1 = 0.231 \pm 0.005$ $\tau_2 = 0.41 \pm 0.01$ $\tau_3 = 0.72 \pm 0.02$ $\tau_4 = 1.10 \pm 0.04$	$\tau_5 = 1.8 \pm 0.1$	$\tau_6 = 5.1 \pm 0.2$	$\tau_7 = 11.0 \pm 0.8$		$\tau_8 = \sim 30$
SA	9	$\tau_1 = 0.245 \pm 0.004$ $\tau_2 = 0.39 \pm 0.01$ $\tau_3 = 0.62 \pm 0.01$ $\tau_4 = 0.96 \pm 0.03$	$\tau_5 = 1.9 \pm 0.1$ $\tau_6 = 3.4 \pm 0.2$		$\tau_7 = 10.7 \pm 0.4$	$\tau_8 = 17.3 \pm 0.6$	$\tau_9 \sim 30$
HMF	8	$\tau_1 = 0.11 \pm 0.06$ $\tau_2 = 0.23 \pm 0.1$ $\tau_3 = 0.36 \pm 0.2$ $\tau_4 = 0.98 \pm 0.7$	$\tau_5 = 2.2 \pm 0.80$ $\tau_6 = 3.6 \pm 0.9$	$\tau_7 = 7.4 \pm 2.3$		$\tau_8 = 21 \pm 7$	

Notes. The standard error is provided for each period. For the last IMF of each record, characterized by one wave, no averages and errors are computed and the approximate time of the single oscillation is provided.

correspond to the averaged square amplitude of IMFs (E_j). IMFs with amplitudes located above the spread line bound contain physical information at that selected confidence level. Figure 4 shows that all the IMFs are significant at the 99th percentile.

These diagrams also allow one to quantify the contribution of each IMF to the global signal. The highest amplitude mode in the CLI data is $j = 8$, having $\tau_8 = 10.6 \pm 0.3$ yr, which can be associated with the 11 yr Schwabe cycle (as a comparison, the highest SA mode is $j = 7$, with $\tau_7 = 10.7 \pm 0.4$ yr), whereas the second most important mode is $j = 9$, having $\tau_9 = 26 \pm 5$ yr, related to the Hale cycle, because its period is comparable with ~22 yr within the error. Indeed, this periodicity represents the highest amplitude mode ($j = 8$, $\tau_8 = 21 \pm 7$ yr) in the HMF magnitude. The CLI mode $j = 7$ ($\tau_7 = 6.5 \pm 0.5$ yr) is found to be the third most prominent mode, while IMFs with τ_j at the typical QBOs timescales (Benevolenskaya 1998; Bazilevskaya et al. 2000, 2006) have lower amplitudes ($j = 4$, $j = 5$, and $j = 6$ with periods $\tau_4 = 1.31 \pm 0.04$ yr, $\tau_5 = 2.19 \pm 0.09$ yr, and $\tau_6 = 3.5 \pm 0.3$, respectively). Mode $j = 10$, with $\tau_{10} \sim 40$ yr, shows only one oscillation, whose τ_j cannot be considered as reliable, given the limited time extent of the data set. Similar results (see Table 1) were obtained for RM and HH data.

For TA data, the highest mode is $j = 7$, with $\tau_7 = 11.0 \pm 0.8$ yr, representing HCS variations in phase with solar activity. Note that a common feature shared by all the data sets, except for SA, is the presence of a high-amplitude IMF at $\tau \sim 6$ yr. In detail, the IMFs $j = 7$ of HH (6.2 ± 0.5) and $j = 6$ of RM ($\tau_6 = 5.6 \pm 0.5$ yr) are found to be the third most prominent mode, as previously found for CLI. Moreover, the second most important mode of the TA and HMF data is $j = 6$ ($\tau_6 = 5.1 \pm 0.2$ yr) and $j = 7$ ($\tau_7 = 7.4 \pm 2.3$ yr), respectively. We remark that the contribution of the ~6 yr mode to the global variability for TA is higher than for HMF, as their energy ratios are $E_6/E_7 = 0.12$ and $E_7/E_8 = 0.01$, respectively. Figure 5 shows that the superposition of the two highest amplitude modes (~11 yr and ~6 yr) for TA and HMF data reproduces quite accurately their global variability.

Finally, modes representing QBOs are found also for TA, SA, and HMF data: $j = 5$ ($\tau_5 = 1.8 \pm 0.1$ yr), $j = 5, 6$ ($\tau_5 = 1.9 \pm 0.1$ yr, $\tau_6 = 3.4 \pm 0.2$ yr), and $j = 5, 6$ ($\tau_5 = 2.2 \pm 0.8$ yr, $\tau_6 = 3.6 \pm 0.9$ yr), respectively.

3. SOLAR MODULATION VERSUS DRIFT EFFECTS

Significant IMFs associated with the 11 yr cycle and QBOs are found for the three CR samples and SA record used in this paper. The QBOs, representing a prominent scale of CR variability, can be obtained by summing up the IMFs in the range between 1.5 and 4 yr. It has been shown (Laurenza et al. 2012) that the superposition of the ~11 yr and QBO contributions accounts for the general features of the CR modulation, such the majority of step-like decreases and the Gnevyshev Gap (GG) phenomenon (Storini & Pase 1995; Storini et al. 2003). The CR variability at these timescales has been associated with solar activity variations (e.g., Vecchio et al. 2012b). The QBOs of CR data were found to be delayed with respect to sunspot activity (Laurenza et al. 2012); the lag was shorter for $A > 0$ periods of even cycles (~1–4 months) than for $A < 0$ ones of odd cycles (~7–9 months). This difference between $A > 0/A < 0$ drift cycles can be explained in terms of the different propagation times experienced by the CRs (e.g., Strauss et al. 2011) with the lag expected to be shorter for $A > 0$ cycles. Figure 6 shows the superposition of the ~11 yr and QBO contribution for the CLI, RM, and HH data (top, middle, and bottom panels, respectively), along with that for SA and TA data. The reconstruction for each CR data set and SA presents a very similar profile, shifted between each other. In particular, the GG is well detected in CR intensity during the maximum phase of all solar cycles and

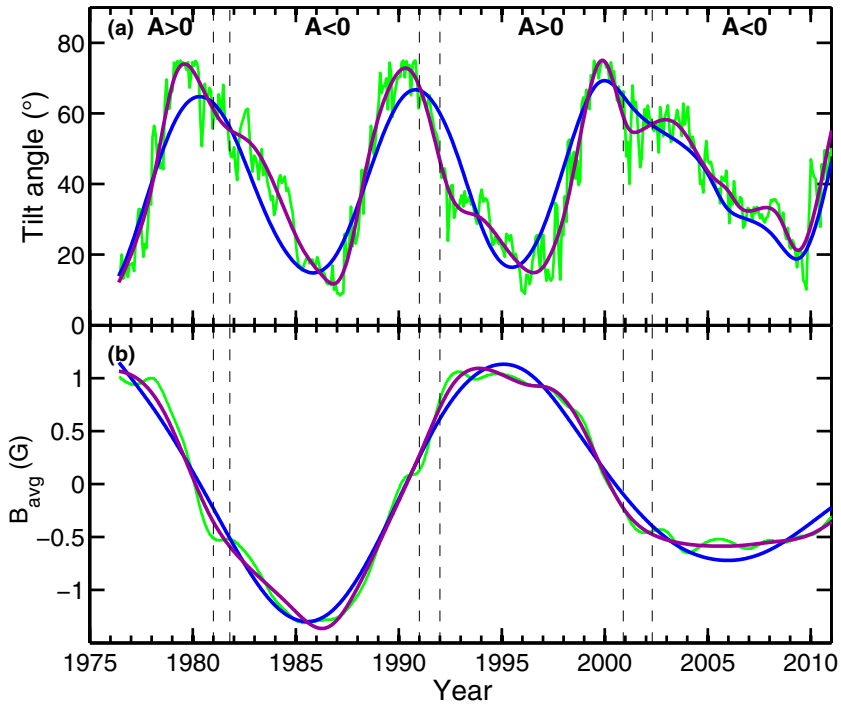

Figure 5. (a) Time history of the HCS TA (green line), ∼11 yr mode (blue line), and the superposition of the ∼11 yr and ∼6 yr modes (violet line), computed from TA data. (b) Time history of the average solar polar field strength (green line) representative for the HMF, ∼22 yr mode (blue line), and the superposition of the ∼22 yr and ∼6 yr modes (violet line), computed from solar polar field strength data. Vertical dashed lines delimit the period when there was no well-defined HMF polarity. The residue, r_m (see the text), is included in each reconstruction.

(A color version of this figure is available in the online journal.)

delayed, with respect to SA, on average of about 6 months. The time lags observed near the sunspot maximum could be due to an efficient diffusion in such periods, when enhanced fluctuations in the magnetic field are expected, while the drift effects should be suppressed (e.g., Minnie et al. 2007). The similarity between the CR and SA profiles confirms that the CR variability, at these timescales, is related to the ∼11 yr solar activity cycle (including QBOs), whose representative index is the SA. The reconstruction performed at these timescales for TA data reflects the SA variability as well, especially the ∼11 yr trend, while the superposed QBOs are less apparent.

The top panels of Figures 7, 8, and 9 compare the variability due to the solar activity with the overall CR variability of the CLI, RM, and HH data. It is apparent that particularly around sunspot minima, i.e., in periods of minimum modulation of Galactic CRs by solar activity, further modes are necessary to explain the variability of the CR flux, i.e., the high-amplitude IMFs with the typical timescales of ∼6 yr and ∼22 yr (see Table 1). The bottom panels of Figures 7, 8, and 9 show two CR signal reconstructions: the first one is obtained by summing up the ∼11 yr and ∼22 yr modes (violet line), whereas the second one also includes the ∼6 yr mode (blue line).

The first reconstruction, where only the effect of the 22 yr mode is considered, shows an enhanced CR flux, with respect to the actual CR data (e.g., the bottom panel of Figure 7) during the $A > 0$ periods, when the magnetic field polarity of the northern solar pole is positive, i.e., outward from the Sun. On the contrary, a reduced CR flux is observed during the $A < 0$ periods. The same behavior is observed also for the RM and HH data (bottom panels of Figures 8 and 9, respectively), although it is less pronounced than for CLI ones. This behavior is accounted for in the transport models for Galactic CRs in the heliosphere (Jokipii et al. 1977; Potgieter 1998, 2013a, and references therein), in which positively charged particles drift in from the heliospheric polar regions during $A > 0$ periods (∼1970–1980 and ∼1990–2000). This result suggests that modes with timescales of ∼22 yr represent the drift effects due to the polarity change of the HMF. On the other hand, the broad (sharp) shape of the CR maxima, during even (odd) numbered sunspot cycles, is entirely determined by the ∼6 yr mode (see the blue line in the bottom panels of Figures 7, 8, and 9), which is found in all of the CR data sets as well as in the TA and HMF records, but not in the SA data. This suggests that the CR variability at the ∼6 yr timescale is not related to solar activity-related perturbations, but to both changes in the HCS inclination and HMF magnitude and hence it can be associated with the CR particle drifts. As a matter of fact, the characteristic period of ∼6 yr is a reasonable average time for the HCS latitudinal excursion from the solar equator to the poles, although its decrease time during the descending phase of the sunspot cycle is usually higher than the rise time, especially for odd numbered cycles (e.g., Cliver & Ling 2001). To a lesser extent, variations at the ∼6 yr scale in HMF intensity influence the CR particle motion both indirectly, by affecting the TA, and directly, by influencing the drift velocities (the lower the HMF magnitude, the larger the drift speeds). Thus, the complete contribution of the drift effects to the CR modulation is included in the CR IMFs at $\tau \sim 6$ yr and 22 yr timescales.

The superpositions of the ∼11 yr and ∼6 yr modes for CLI, RM, HH (blue lines), as well as for the TA (magenta line) are shown in Figures 10, 11, and 12, respectively. For all the CR data, a noticeable anticorrelation is observed, i.e., the slow decrease of the TA during the descending phase of odd solar cycles is reflected in a low CR penetration. At the same time, the rapid increase of the TA during the rise phases produces sharp CR profiles. Nevertheless, small-scale features present

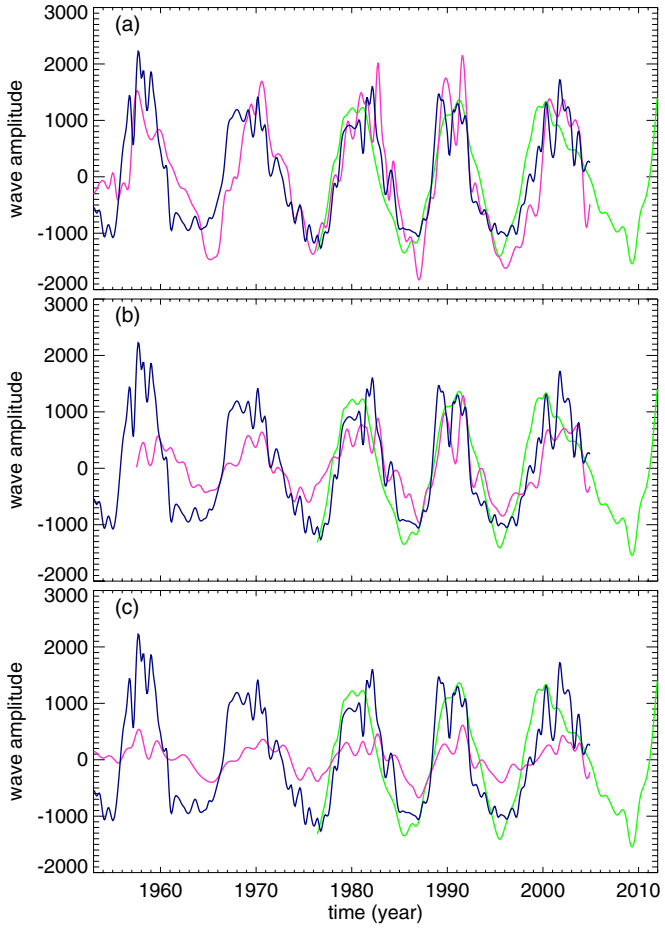

Figure 6. (a) Superposition of the ∼11 yr mode and the QBOs computed from SA (blue), CLI (magenta), and TA (green) data. (b) Same as panel (a) for RM data. (c) Same as panel (a) for HH data. CR results are inverted and rescaled by a constant factor equal to 200. The TA result is rescaled by a constant factor equal to 50.

(A color version of this figure is available in the online journal.)

in the TA reconstruction (e.g., the inflection points around 1980–1981, 1991, and 2003) are not always reflected in the CR ones. For instance, in CLI data, only the inflection in 1991 is detected when the TA is relatively small, between 39.°5 and 35° (Figure 10). On the contrary, when the HCS is at high latitudes (i.e., in 1980–1981 and 2003), the CR intensity seems not to be affected. On the other hand, the two small-scale features observed at higher values of the TA, as in 1980–1981 when it is between 50° and 43.°5 or in 1999–2000 when it is between 53.°17 and 56.°5, are both reproduced in the HH data (Figure 12). As far as the RM data are concerned, only the former inflection point is present, i.e., for mid-latitude values of the TA (see Figure 11). Note that the RM neutron monitor has an intermediate rigidity cutoff between CLI and HH. This suggests the existence of a threshold for the TA, depending on CR energy, below which the CR flux is strongly modulated by HCS variations. Above the threshold, the CR flux is strongly decreased, despite the TA variations. The threshold for the three CR data sets is found to be at ∼40°, ∼45°, and >56.°5 for CLI, RM, and HH, respectively, with a cut-off rigidity of ∼3.0 GV, ∼6.3 GV, and ∼12.9 GV, respectively. In particular, Figure 12 shows that the HH CR flux is sensitive to TA variations even at about 60°. The TA threshold effect could be due to the disruption of the drift process when the TA increases, as proposed by Strauss et al. (2012).

Table 2
Evaluation of the Amplitude of the Most Important Modes with Respect to the Global Signal for Each CR Sample

Parameter	6 yr mode	11 yr mode	22 yr mode
CLI	0.09	0.52	0.25
RM	0.10	0.48	0.25
HH	0.11	0.45	0.20

3.1. Estimation of Drift Effects

The EMD allows one to quantify the relative contribution of the CR drift- and solar activity-associated modes to the total CR modulation. The contribution of each mode to the global variability can be evaluated by computing the normalized mean-square amplitude:

$$\frac{\langle|\psi_j(t)|^2\rangle}{\sum_{j=1}^{N}\langle|\psi_j(t)|^2\rangle}, \quad (5)$$

where $\langle , \rangle$ denotes the time average over the whole considered period. This quantity was calculated for the ∼11 yr, ∼22 yr, and ∼6 yr modes, for each CR sample, as reported in Table 2. As expected, the main contribution (∼50%) to the CR modulation is due to the 11 yr solar cycle for all cases. The effect of the HCS latitudinal extent and/or the drift velocity variations can be estimated to be ∼10% while that of the polarity inversion is estimated to be 20%–25% depending on the CR particle energy.

The contribution of the drift-associated modes to the total modulation cannot be computed as a function of time by applying Equation (5), because the orthogonality is not generally guaranteed in localized time intervals. A first evaluation of the importance of the drift effects in time can be obtained from the superposition of the ∼6 and ∼22 yr IMFs, hereafter $D(t)$, for the CLI, RM, and HH records. The time behavior of $D(t)$ is shown in panel a of Figure 13. Moreover, the superposition of the most important modes of the TA (∼6 yr and ∼11 yr) and the HMF magnitude (∼6 yr and ∼22 yr) is illustrated in panel b of Figure 13, to understand how the behavior of the CR drift-associated modes is related to the time variations of the TA and HMF. For the three CR data sets, $D(t)$ presents a similar shape with different amplitudes, depending on the different CR energy involved. The $D(t)$ amplitude is always negative when the HMF magnitude is negative, i.e., during $A < 0$ periods, indicating that the drift-associated modes always reduce the CR flux in such periods. This reflects that CR particles, drifting inward along the HCS, undergo more modulation. The highest negative $D(t)$ amplitudes are observed when the TA is quite high and the HMF moderately low. On the other hand, when the HMF magnitude is positive, during $A > 0$ periods, the $D(t)$ amplitude is positive, i.e., the modes at ∼6 yr and ∼22 yr affect the CR time profile, increasing their flux with respect to the average value over the whole period. This corresponds to a more efficient CR particles transport toward the Earth as they drift from the polar regions. For instance, the prompt rise of the CR flux after 1970 (see Figure 7) is determined by the high $D(t)$ amplitude in the same period as shown in Figure 13. On the other hand, the $D(t)$ amplitude tends to be zero or low during some periods (e.g., 1956–1957, 1968–1970, 1979–1981, and 1992) nearing the sunspot maximum (generally close to the HMF polarity inversions), apart from solar cycle 22.

These observations demonstrate that the HCS elevation is critical in determining drift effects on the CR modulation. In particular, the HCS elevation determines the shape of $D(t)$, i.e., large decreases (increases) are found corresponding to

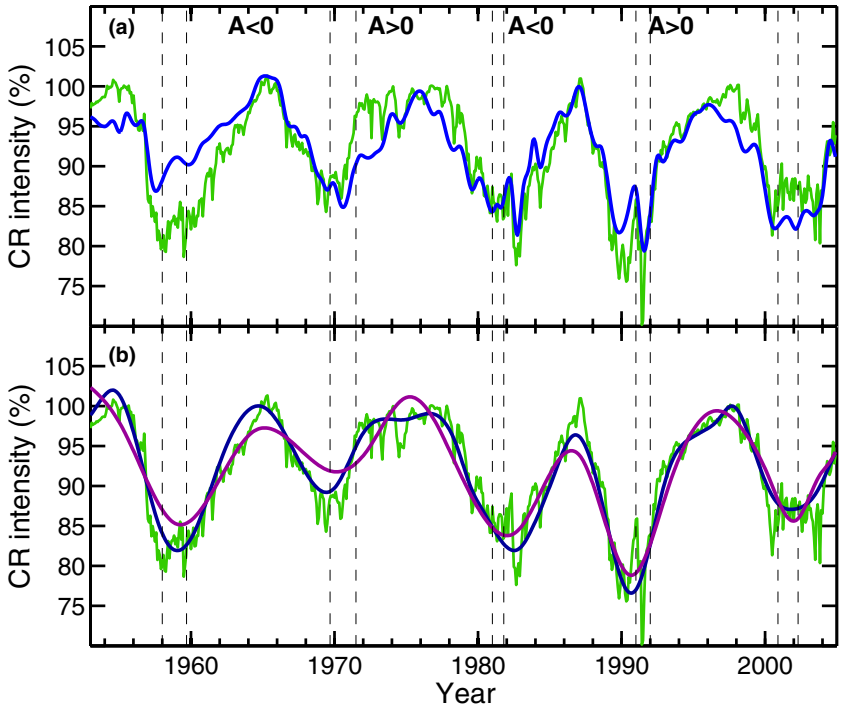

Figure 7. (a) CR intensity (green line) and superposition of the ∼11 yr and ∼2 yr modes (blue line) computed from CLI data. (b) CR intensity (green line), superposition of the ∼11 yr and ∼22 yr modes (violet line), and superposition of the ∼11 yr, ∼22 yr, and ∼6 yr modes (dark blue line), computed from CLI data. Vertical dashed lines delimit the short period when there was no well-defined HMF polarity. The residue r_m (see the text) is included in each reconstruction.

(A color version of this figure is available in the online journal.)

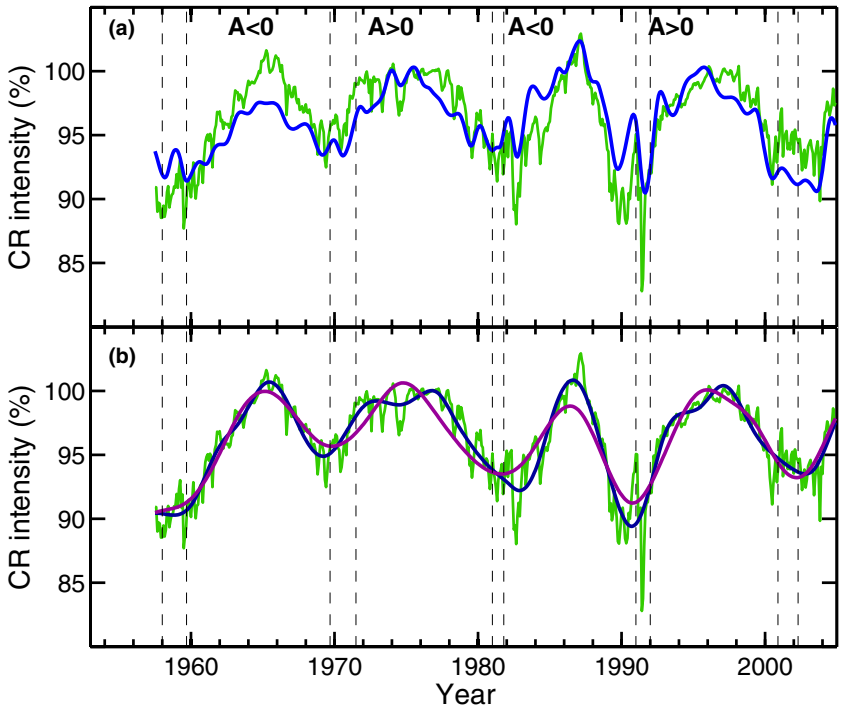

Figure 8. (a) CR intensity (green line) and superposition of the ∼11 yr and ∼2 yr modes (blue line) computed from RM data. (b) CR intensity (green line), superposition of the ∼11 yr and ∼22 yr modes (violet line), and superposition of the ∼11 yr, ∼22 yr, and ∼6 yr modes (dark blue line), computed from RM data. Vertical dashed lines delimit the short period when there was no well-defined HMF polarity. The residue r_m (see the text) is included in each reconstruction.

(A color version of this figure is available in the online journal.)

high (low) TAs. As far as the HMF is concerned, its polarity determines the sign of $D(t)$, while amplitude variations seems to be less relevant in affecting the drift effects. Note that RM differs from other data sets during cycle 19. Possible explanations could involve the equatorial viewing directions of the RM observatory and/or EMD border effects, which affect the detection of long periodicities at the data set limits (the starting date of the RM data is 1957 June, very close to the maximum phase of cycle 19). Unfortunately, no records of the TA and HMF are available for that period to discuss in detail this difference.

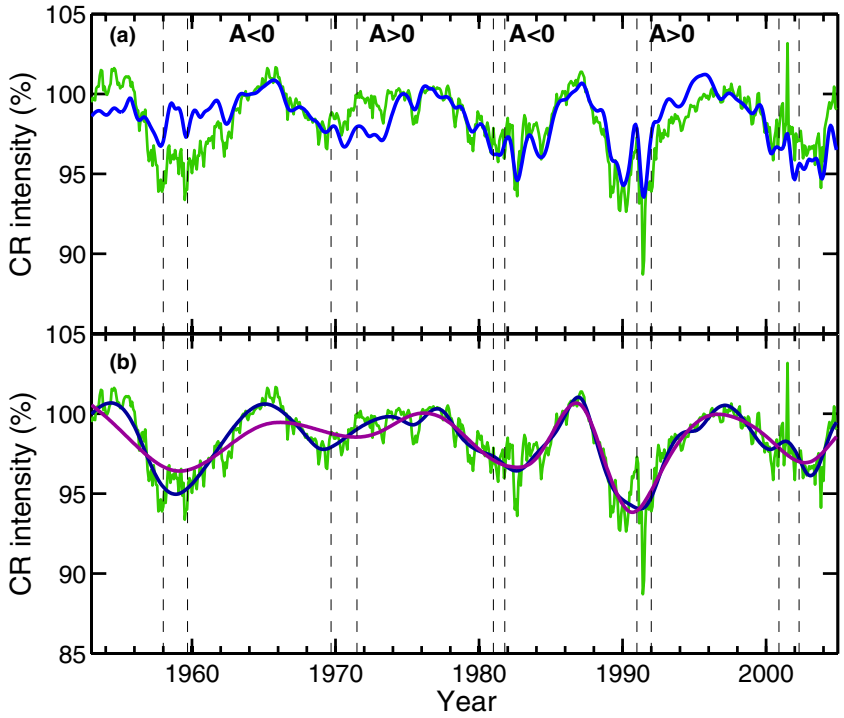

Figure 9. (a) CR intensity (green line) and superposition of the ∼11 yr and ∼2 yr modes (blue line) computed from HH data. (b) CR intensity (green line), superposition of the ∼11 yr and ∼22 yr modes (violet line), and superposition of the ∼11 yr, ∼22 yr, and ∼6 yr modes (dark blue line), computed from HH data. Vertical dashed lines delimit the short period when there was no well-defined HMF polarity. The residue r_m (see the text) is included in each reconstruction.

(A color version of this figure is available in the online journal.)

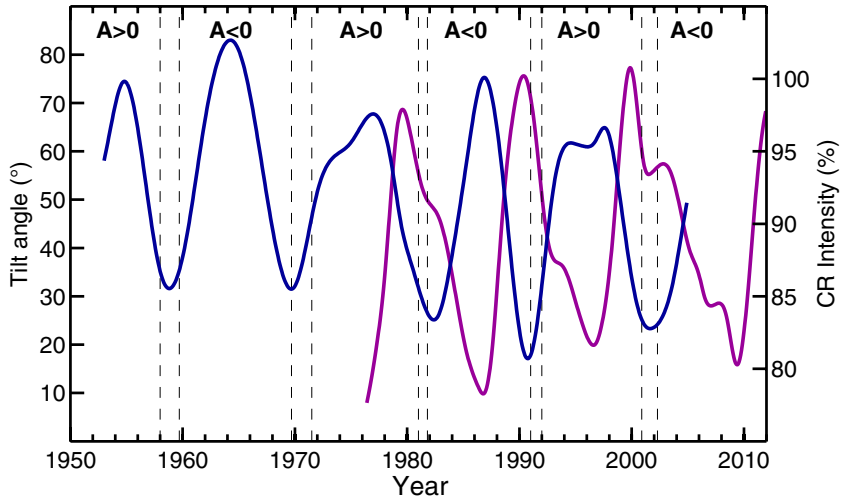

Figure 10. Superposition of the ∼11 yr and ∼6 yr modes computed from CLI (blue line) and TA (magenta line) data. The residue r_m (see the text) is included in each reconstruction.

(A color version of this figure is available in the online journal.)

In order to quantify the drift contribution to the total modulation in different time intervals, we use the Hilbert transform, defined in Section 2. After performing the Hilbert transform on each IMF component, the original time series can be expressed in the following form:

$$\Psi(t) = \sum_{j=1}^{m} A_j(t) \exp\left(i \int \omega_j(t) dt\right) + r_m(t). \quad (6)$$

Equation (6) allows one to represent amplitude and instantaneous frequency for each mode as function of time (see also Equations (3) and (4)). The frequency–time distribution of the amplitude is called the "Hilbert amplitude spectrum," $H(\omega, t)$ (Huang et al. 1998). For our purposes, we exclude the residue from Equation (6); since we are interested in the information content of the oscillating components, the non-IMF components can be left out. This is equivalent to calculating a partial reconstruction without using $r_m(t)$. The contribution of the drift-associated modes to the total modulation in the time interval $[t_1, t_2]$ can be thus calculated through the parameter p:

$$p = \int_{\omega_1}^{\omega_2} \int_{t_1}^{t_2} H(\omega, t) d\omega dt \Big/ \int_{\omega} \int_{t_1}^{t_2} H(\omega, t) d\omega dt, \quad (7)$$

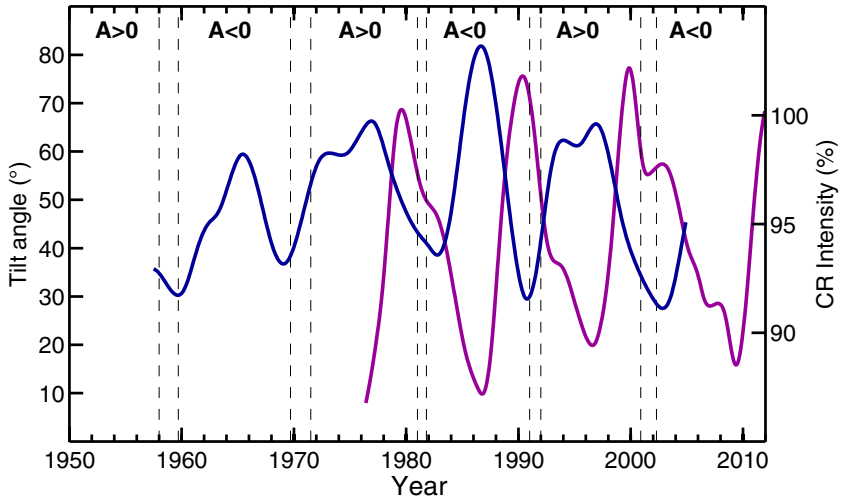

Figure 11. Superposition of the ∼11 yr and ∼6 yr modes computed from RM (blue line) and TA (magenta line) data. The residue r_m (see the text) is included in each reconstruction.

(A color version of this figure is available in the online journal.)

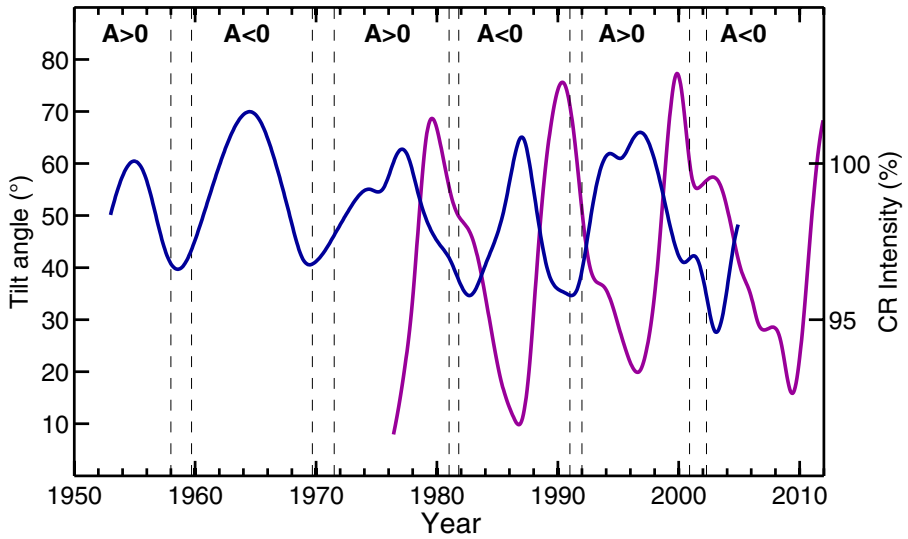

Figure 12. Superposition of the ∼11 yr and ∼6 yr modes computed from HH (blue line) and TA (magenta line) data. The residue r_m (see the text) is included in each reconstruction.

(A color version of this figure is available in the online journal.)

where the integrals at the denominator are extended over the whole frequency range. We integrate Equation (7) between $\omega_1 = 0.95\ \mathrm{yr}^{-1}$ and $\omega_2 = 1.14\ \mathrm{yr}^{-1}$ to obtain the contribution of the modes with timescales of ∼6 yr and between $\omega_1 = 0.14\ \mathrm{yr}^{-1}$ and $\omega_2 = 0.35\ \mathrm{yr}^{-1}$ to get the contribution of the modes with timescales around 22 yr. The total p, accounting for the full drift contribution, is obtained by summing up the two results. We remark that, when computing p over the whole time period and in the above frequency ranges, we obtain the same results computed through Equation (5) listed in the first and third column of Table 2.

The parameter p has been computed in selected time intervals where there is no well defined HMF polarity, as has been reported in the literature (Makarov & Sivaraman 1986; Bazilevskaya et al. 2000; Gopalswamy et al. 2003). Values are listed in Table 3, which also indicates the sign (plus or minus) of the mean drift-associated mode in the considered time interval. In case of a negative sign, the superposition of the drift-associated modes produces a decrease of the CR flux. In general, we observe a decrease of the drift contribution for higher energy particles, being the p values are lower for HH than RM and CLI and a sign coherence is observed among the three data sets. Moreover, the obtained values for the drift contribution are generally lower than those computed for the whole period (0.34, 0.37, and 0.31 for CLI, RM, and HH data, respectively; see Table 2), indicating that the drift effects are decreased during the solar maxima, as proposed by Ndiitwani et al. (2005).

Table 3
Values of p as Computed in Periods of no Definite Polarity for Each CR Sample

Time Interval	CLI	RM	HH
1958.0–1959.7	0.32 (−)	0.21 (−)	0.22 (−)
1969.7–1971.5	0.40 (+)	0.26 (+)	0.23 (+)
1981.0–1981.8	0.16 (−)	0.21 (−)	0.21 (−)
1991.0–1992.0	0.27 (−)	0.21 (−)	0.14 (−)
2000.9–2002.3	0.22 (+)	0.21 (+)	0.14 (+)

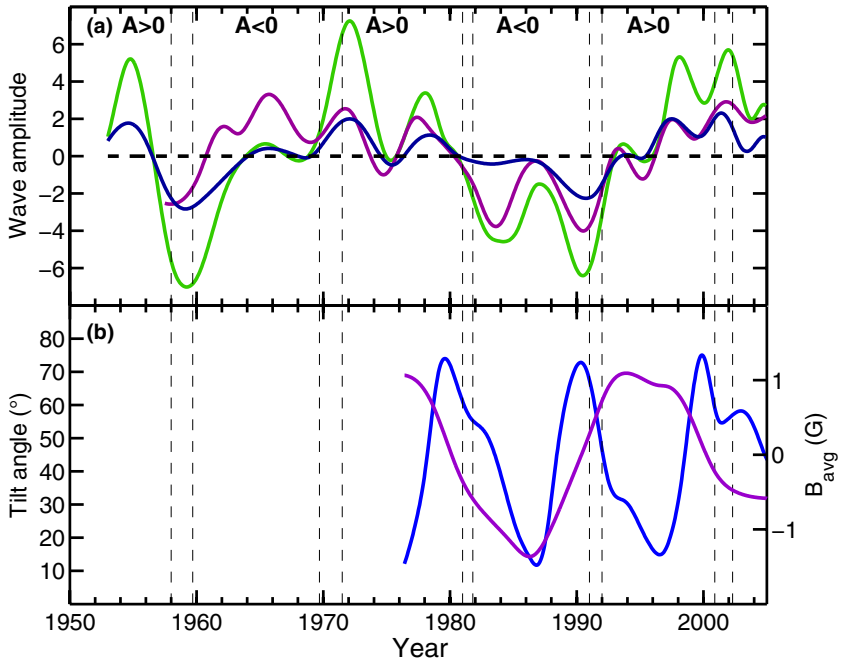

Figure 13. (a) Superposition of the ∼6 yr and ∼22 yr modes computed from CLI (green line), RM (magenta line), and HH (blue line) data. (b) Superposition of the ∼6 yr and ∼11 yr modes computed from TA data (blue line) and ∼6 yr and ∼22 yr modes computed from the solar polar field strength representative for the HMF magnitude (violet line).

(A color version of this figure is available in the online journal.)

4. CONCLUSIONS

In this paper, we investigated the drift effects on the CR modulation. To this end, we used the EMD to analyze the time variability of the CR intensity (measured by CLI, RM, and HH neutron monitors), the HCS, TA, and the HMF magnitude. Moreover, the SA was selected as an index of solar activity related to interplanetary perturbations affecting the CR flux. Since the EMD allows one to characterize a given signal with modes having well-defined and separated timescales, we were able to identify the different causes producing the CR modulation and quantify their relative contributions to the variability of each CR signal. By comparing EMD modes of TA, HMF magnitude, and SA with CR ones at similar timescales, the modulation effects due to the solar activity from those related with the particle drifts have been determined. The solar magnetic activity was found to be responsible for the well-known 11 yr variation, the GG phenomenon, and most of the step-like CR decreases through the combined action of the 11 yr mode and QBO ones. On the other hand, the drift effects have been associated with variations at ∼22 yr and ∼6 yr. The ∼22 yr mode detected in CR data has been related to the changes in the polarity state of the heliosphere, as it is the most important mode in the HMF magnitude. In particular, the effect of the 22 yr mode is found to enhance (decrease) the CR flux, when compared with the actual data, during periods of positive (negative) polarity in the northern hemisphere. This effect, which is more pronounced for low-energy CRs, can be explained in terms of the different access of the positive charged particles in the inner heliosphere (from polar/equatorial regions during $A > 0/A < 0$ semicycles), as expected from drift theory.

The ∼6 yr mode is found to be responsible for the peaked (flat) topped maximum feature observed in the CR intensity during odd (even) numbered cycles. The CR behavior at ∼6 yr can be understood from results obtained through the EMD decomposition of the HCS TA and HMF data. The main scale of TA variability is the ∼11 yr mode, due to the solar activity, followed by a ∼6 yr variation, being their ratio equal to 0.12. The ∼6 yr mode is also the second prominent mode in the HMF magnitude, although the ratio with respect to the main ∼22 yr mode is much lower (0.01). On the contrary, the ∼6 yr periodicity is not observed in solar parameters such as the SA. Hence, this mode cannot be associated with activity phenomena on the Sun, but can be associated with changes in the HCS inclination, as the average time for its latitudinal excursion is about 6 yr. The ∼6 yr scale of CR variability also includes, to a lesser extent, the effect of the HMF variation at the same timescale, which can affect the drift velocities.

It has been proposed that a systematic variation of the TA modulates the CR flux either via drifts, as a result of the TA difference itself, or as a consequence of the different latitude distribution of coronal mass ejections between even and odd cycles (Cliver et al. 1996; Cliver & Ling 2001). Our results show for the first time that the CR modulation at the ∼6 yr timescale exactly matches the corresponding variation in the TA, favoring the former hypothesis, i.e., that the HCS latitudinal excursion affects the CR flux, via drift processes on the CR particles. Moreover, we observe a critical threshold, under which the CR flux is strongly affected by the HCS variations, for the TA: ∼40° at CLI CR energy, ∼45° at RM, and greater than 55° at HH ones. When the TA inclination is higher than the obtained threshold, the CR flux is noticeably reduced and not sensitive to any TA fluctuations. Note that the higher the threshold, the higher the CR energy, possibly because of the larger Larmor radius of the high-energy particles that are able to explore high latitudes.

In conclusion, our analysis assesses that the occurrence of flat-topped CR maxima during alternate even-odd sunspot cycles is due to the drift effects mainly related to the TA latitude variations. This result represents clear experimental evidence for the validity of the drift models, including the wavy HCS

(e.g., Kota & Jokipii 1983; Potgieter 2013a; Strauss et al. 2011; Kota 2012). Finally, a quantitative estimation is provided for modulation induced by solar activity and by drifts. The former contribution to the CR global modulation is between 52% and 45%, decreasing with increasing CR energy. The full contribution of the drifts (including both TA variations and polarity reversals) to the CR global modulation is between 0.30 and 0.35, increasing with decreasing CR energy. The individual contributions at ∼6 yr and ∼22 yr variations are estimated to be about 0.10 and 0.20–0.25, respectively. Results of the variation in time of the total drift contribution show that it is almost zero in some periods nearing the sunspot maximum. Moreover, during periods of no well-defined polarity of the solar magnetic field, in the sunspot maximum phase, the drift contribution to the CR modulation is estimated to be generally less than 0.30 (see Table 3), reduced with respect to its value over the whole period, which is in good agreement with Ndiitwani et al. (2005) and Minnie et al. (2007).

This work was partially supported by the ASI/INAF contract no. I/022/10/0. Thanks are due also to the Italian PNRA for the use of the RAC-ANT database, prepared at the former IFSI-Roma (now IAPS) under contract PROGDEF09 37 (code 2009/A3.07). The authors thank the referee for insightful comments.

REFERENCES

Alanko-Huotari, K., Usoskin, I. G., Mursula, K., & Kovaltsov, G. A. 2007, JGR, 112, A08101
Badruddin, Singh, M., & Singh, Y. P. 2007, A&A, 466, 697
Bazilevskaya, G. A., Krainev, M. B., Makhmutov, V. S., et al. 2000, SoPh, 197, 157
Bazilevskaya, G. A., Makhmutov, V. S., & Sladkova, A. I. 2006, AdSpR, 38, 484
Benevolenskaya, E. E. 1998, ApJL, 509, L49
Christon, S. P., & Stone, E. C. 1986, GeoRL, 13, 777
Cliver, E. W., Boriakoff, V., & Bounar, K. H. 1996, JGR, 101, 27091
Cliver, E. W., & Ling, A. G. 2001, ApJ, 556, 432
Cummings, D. A. T., Irizarry, R. A., Huang, N. E., et al. 2004, Natur, 427, 344
El-Borie, M. A. 2001, APh, 16, 169
Ferreira, S. E. S., & Potgieter, M. S. 2004, ApJ, 603, 744
Forbush, S. E. 1954, JGR, 59, 525
Forbush, S. E. 1966, HDP, 49, 159
Gopalswamy, N., Lara, A., Yashiro, S., & Howard, R. A. 2003, ApJL, 598, L63
Hess, V. F. 1912, PhyZ, 13, 1084
Hoeksema, J. T. 1989, AdSpR, 9, 141
Hoeksema, J. T., Wilcox, J. M., & Scherrer, P. H. 1982, JGR, 87, 10331
Huang, N. E., Shen, Z., Long, S. R., et al. 1998, RSPSA, 454, 903
Jiang, J., Cameron, R., Schmitt, D., & Schüssler, M. 2010, ApJ, 709, 301
Jokipii, J. R., Levy, E. H., & Hubbard, W. B. 1977, ApJ, 213, 861
Jokipii, J. R., & Thomas, B. 1981, ApJ, 243, 1115
Kota, J. 2012, SSRv, 176, 391
Kota, J., & Jokipii, J. R. 1983, ApJ, 265, 573
Laurenza, M., Vecchio, A., Storini, M., & Carbone, V. 2012, ApJ, 749, 167
Le Roux, J. A., & Potgieter, M. S. 1992a, ApJ, 390, 661
Le Roux, J. A., & Potgieter, M. S. 1992b, ApJ, 397, 686
Makarov, V. I., & Sivaraman, K. R. 1986, BASI, 14, 163
Manuel, R., Ferreira, S. E. S., Potgieter, M. S., Strauss, R. D., & Engelbrecht, N. E. 2011, AdSpR, 47, 1529
Minnie, J., Bieber, J. W., Matthaeus, W. H., & Burger, R. A. 2007, ApJ, 670, 1149
Ndiitwani, D. C., Ferreira, S. E. S., Potgieter, M. S., & Heber, B. 2005, AnG., 23, 1061
Potgieter, M. S. 1998, SSRv, 83, 147
Potgieter, M. S. 2013a, SSRv, 176, 165
Potgieter, M. S. 2013b, SSRv, 10, 3
Potgieter, M. S., & Ferreira, S. E. S. 2001, AdSpR, 27, 481
Potgieter, M. S., & Le Roux, J. A. 1992, ApJ, 392, 300
Smith, E. J. 1990, JGR, 95, 18731
Storini, M. 1990, NCimC, 13, 103
Storini, M. 1997, NCimC, 20, 871
Storini, M., Bazilevskaya, G. A., Fluckiger, E. O., et al. 2003, AdSR, 31, 895
Storini, M., & Pase, S. 1995, in Proc. Second SOLTIP Symp., ed. T. Watanabe (STEP GBRSC News, Vol. 5, Special Issue; Mito, Japan: Ibaraki Univ.), 255
Strauss, R. D., Potgieter, M. S., Büsching, I., & Kopp, A. 2012, Ap&SS, 339, 223
Strauss, R. D., Potgieter, M. S., Kopp, A., & Büsching, I. 2011, JGR, 116, A12105
Terradas, J., Oliver, R., & Ballester, J. L. 2004, ApJ, 614, 435
Torrence, C., & Compo, G. P. 1998, BAMS, 79, 61
Vecchio, A., Laurenza, M., Carbone, V., & Storini, M. 2010, ApJL, 709, L1
Vecchio, A., Laurenza, M., Meduri, D., Carbone, V., & Storini, M. 2012a, ApJ, 749, 27
Vecchio, A., Laurenza, M., Storini, M., & Carbone, V. 2012b, AdAst, 2012, 834247
Wibberenz, G., Cane, H. V., Richardson, I. G., & von Rosenvinge, T. T. 2001, SSRv, 97, 343
Wu, Z., & Huang, N. E. 2004, RSPSA, 460, 1597